Near-Field Full-Duplex Integrated Sensing and Communication with Dynamic Metasurface Antennas

Murat Bayraktar*, Nuria González-Prelcic*, Hao Chen†, Charlie Jianzhong Zhang†
*University of California San Diego, USA
†Standards and Mobility Innovation Lab, Samsung Research America, USA
Email:{mbayraktar,ngprelcic}@ucsd.edu, {hao.chen1,jianzhong.z}@samsung.com

***Abstract*—A full duplex (FD) multiple-input multiple-output (MIMO) communication system can also provide monostatic sensing capabilities by processing the echoes of the downlink (DL) signal or by dedicating specific spatial resources to sensing. This integrated sensing and communication (ISAC) setting requires the design of precoders and combiners at the FD base station (BS) to balance sensing and communication performance while suppressing the self-interference (SI) caused by simultaneous transmission and reception. Although this subject has been studied for conventional arrays that operate in the far-field (FF), near-field (NF) FD-ISAC is still in its nascent stages. Given that the extremely large arrays to be used in high frequency bands and in the upper mid-band will lead to operation in the NF for many users, it is essential to design techniques for NF FD-ISAC. In this paper, we tackle the design of the precoders and combiners that enable NF FD-ISAC while exploiting dynamic metasurface antennas (DMAs) at the BS. We evaluate our design considering sensing and communication metrics, in addition to its SI mitigation capability.**

***Index Terms*—Near-field communication, full-duplex communication, integrated sensing and communication, dynamic metasurface antennas.**

I. INTRODUCTION

Integrated sensing and communication (ISAC) has emerged as a promising technology for future wireless networks [1]. One of the potential ISAC configurations focuses on a monostatic sensing mode exploiting a full-duplex (FD) circuit for simultaneous downlink (DL) communication and target sensing leveraging the reflected signals [2]. The design of FD-ISAC systems introduces significant challenges due to the effects of the self-interference (SI) inherent to FD operation. Specifically, the SI must be suppressed before the signal reaches the low-noise amplifiers (LNAs) and the analog-to-digital converters (ADCs) of the receiver (RX) side of the FD node. It has been shown that the precoders and analog combiners at a base station (BS) can be designed to enable ISAC operation under SI constraints for systems that employ multiple-input multiple-output (MIMO) architectures [3]–[5].

Extremely large MIMO systems, anticipated to operate at sub-THz and upper mid-band frequencies, offer high angular resolution, which is particularly beneficial for ISAC applications. However, the large array apertures at these frequency bands will lead to near-field (NF) operation both for communication and sensing. While the design of precoders and combiners for far-field (FF) FD-ISAC systems has been explored in previous work [3]–[5], research on NF FD-ISAC remains in its infancy [6]–[8].

Dynamic metasurface antennas (DMAs) can provide low-cost alternative to extremely large arrays for both communication [9]–[11] and sensing applications [12], [13]. DMA architectures utilize microstrips composed of meta-elements, whose responses can be controlled through passive circuitry. Recently, DMAs have been explored for NF FD ISAC applications at sub-THz frequencies [14], [15]. However, these studies neglect the attenuation inside microstrips, and design the DMA weights based on a DFT codebook, which violates the Lorentzian constraint required by the DMAs. The resulting unit-modulus weights from the DFT codebook are subsequently projected onto the Lorentzian-constrained set to overcome this limitation.

This paper addresses the optimization of DMA weights for a NF FD-ISAC system. We propose a novel precoding and combining strategy to suppress SI while enabling communication and sensing functionalities, adhering to the Lorentzian constraint of the DMA weights. The optimization of the transmit (TX) and RX DMA weights are reformulated as unconstrained problems on a Riemannian manifold, which are efficiently solved using a conjugate gradient descent algorithm. Numerical results show that the proposed method outperforms the benchmark in both sub-THz and upper mid-band settings.

II. SYSTEM MODEL

In this paper, we consider an FD-ISAC system with colocated TX and RX DMAs as depicted in Fig. 1. Since the TX and RX DMAs are placed close to each other, the RX side observes a strong SI. The microstrips of the DMAs lie on the x-axis while multiple microstrips are placed in parallel in the z-axis. Without loss of generality, both the TX and RX DMAs comprise N_d microstrips each of which containing N_e meta-elements. Thus, the number of elements at both sides are denoted by $N = N_\mathrm{d}N_\mathrm{e}$. Note that each microstrip is connected to a radio frequency (RF) chain. We consider K targets in the NF of the DMAs. We assume that one of the targets is also a UE that utilizes a fully digital N_u-antenna uniform linear array (ULA). The FD-ISAC system transmits the DL communication signals to the UE while simultaneously receiving the reflected echoes. We consider a tracking scenario such that a prior estimate of the target locations are available.

This material is based upon work supported in part by the National Science Foundation under grant no. 2433782 and is supported in part by funds from the federal agency and industry partners as specified in the Resilient & Intelligent NextG Systems (RINGS) program and in part by Samsung Research America.

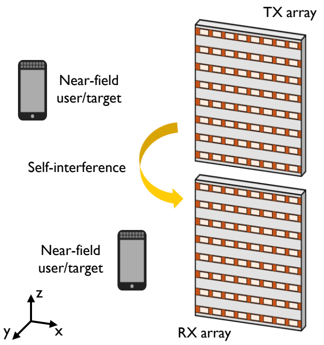

Fig. 1. The DMA-based FD-ISAC system operating in the NF.

A. Channel Models

In the following, we introduce the channel models used for DL communication, target reflections and SI. We consider a narrowband operation since the bandwidth of the system is limited. Furthermore, we assume that the channels follow the NF line-of-sight (LoS) channel model. The DL channel between the TX DMA and the UE is denoted by $\mathbf{H}_{\mathrm{u}} \in \mathbb{C}^{N_{\mathrm{u}} \times N}$. The locations of the n-th UE antenna and the i-th element of the j-th TX DMA microstrip are denoted by $\mathbf{r}_{\mathrm{u},n} \in \mathbb{R}^{3\times 1}$ and $\mathbf{r}_{\mathrm{TX},i,j} \in \mathbb{R}^{3\times 1}$, respectively. With this definition, the channel response between the i-th element of the j-th TX DMA microstrip and the n-th UE antenna is expressed as

$$[\mathbf{H}_{\mathrm{u}}]_{n,(j-1)N_{\mathrm{e}}+i} = A(\mathbf{r}_{\mathrm{u},n}, \mathbf{r}_{\mathrm{TX},i,j}) e^{-\jmath\frac{2\pi}{\lambda}\|\mathbf{r}_{\mathrm{u},n}-\mathbf{r}_{\mathrm{TX},i,j}\|}, \quad (1)$$

where λ is the wavelength and $A(\mathbf{r}_{\mathrm{u},n}, \mathbf{r}_{\mathrm{TX},i,j})$ is the complex channel gain that depends on the relative positions of the elements. The complex channel gain is defined as

$$A(\mathbf{r}_{\mathrm{u},n}, \mathbf{r}_{\mathrm{TX},i,j}) = \frac{\lambda\sqrt{F(\theta_{\mathrm{u},i,j,n}, \phi_{\mathrm{u},i,j,n})}}{4\pi\|\mathbf{r}_{\mathrm{u},n} - \mathbf{r}_{\mathrm{TX},i,j}\|} e^{-\frac{\kappa_{\mathrm{abs}}\|\mathbf{r}_{\mathrm{u},n}-\mathbf{r}_{\mathrm{TX},i,j}\|}{2}}, \quad (2)$$

where $\theta_{\mathrm{u},i,j,n}$ and $\phi_{\mathrm{u},i,j,n}$ are the azimuth and elevation angles of the n-th UE antenna with respect to the i-th element of the j-th TX DMA microstrip. Furthermore, $F(\theta, \phi)$ is the radiation pattern of the meta-elements for some given azimuth angle θ and elevation angle ϕ. While the radiation pattern depends on the specific DMA technology, we utilize the commonly used model in [16]. Finally, κ_{abs} is the atmospheric absorption coefficient which is prominently observed at the sub-THz and the THz band, and can be neglected at lower frequencies. Analogously, the target channel comprising the reflections from K targets is denoted by $\mathbf{H}_{\mathrm{R}} \in \mathbb{C}^{N\times N}$. The channel response between the i-th element of the j-th TX DMA microstrip and the i'-th element of the j'-th RX DMA microstrip is expressed as

$$\begin{aligned}[\mathbf{H}_{\mathrm{R}}]_{(j'-1)N_{\mathrm{e}}+i',(j-1)N_{\mathrm{e}}+i} &= \sum\nolimits_{k=1}^{K} \beta_k A(\mathbf{r}_k, \mathbf{r}_{\mathrm{TX},i,j}) \\ &\times A(\mathbf{r}_k, \mathbf{r}_{\mathrm{RX},i',j'}) e^{-\jmath\frac{2\pi}{\lambda}\left(\|\mathbf{r}_k-\mathbf{r}_{\mathrm{TX},i,j}\|+\|\mathbf{r}_k-\mathbf{r}_{\mathrm{RX},i',j'}\|\right)}, \quad (3)\end{aligned}$$

where the magnitude of the complex scattering coefficient of the k-th target, β_k, is given by $|\beta_k| = \sqrt{4\pi\nu_k}/\lambda$, with ν_k the radar cross-section of the k-th target. Additionally, the location of the i'-th element of the j'-th RX DMA microstrip is denoted by $\mathbf{r}_{\mathrm{RX},i',j'} \in \mathbb{R}^{3\times 1}$. The SI channel, $\mathbf{H}_{\mathrm{SI}} \in \mathbb{C}^{N\times N}$, can be modeled in a similar way to the DL channel. The SI channel response between the i-th element of the j-th TX DMA microstrip and the i'-th element of the j'-th RX DMA microstrip is expressed as

$$\begin{aligned}[\mathbf{H}_{\mathrm{SI}}]_{(j'-1)N_{\mathrm{e}}+i',(j-1)N_{\mathrm{e}}+i} &= A(\mathbf{r}_{\mathrm{RX},i',j'}, \mathbf{r}_{\mathrm{TX},i,j}) \\ &\times e^{-\jmath\frac{2\pi}{\lambda}\|\mathbf{r}_{\mathrm{RX},i',j'}-\mathbf{r}_{\mathrm{TX},i,j}\|}. \quad (4)\end{aligned}$$

B. Received Signal Models

The TX side of the FD BS transmits the DL signal $\mathbf{x} \in \mathbb{C}^{N_{\mathrm{s}}\times 1}$, with $N_{\mathrm{s}} \leq \min(N_{\mathrm{u}}, N_{\mathrm{d}})$ data streams that satisfy $\mathbb{E}\{\mathbf{x}\mathbf{x}^{\mathrm{H}}\} = \mathbf{I}$. The DL signal passes through several stages: (i) digital precoder $\mathbf{V} \in \mathbb{C}^{N_{\mathrm{d}}\times N_{\mathrm{s}}}$; (ii) TX DMA weights $\mathbf{F} \in \mathbb{C}^{N\times N_{\mathrm{d}}}$; and (iii) diagonal TX attenuation matrix $\mathbf{P}_{\mathrm{TX}} \in \mathbb{C}^{N\times N}$. The entries of the digital precoder $\mathbf{V}$ can be freely chosen, while the DMA weights are constrained by hardware. Considering that each DMA is connected to a separate RF chain, the weight matrix $\mathbf{F}$ has a block-diagonal structure given as $\mathbf{F} = \mathrm{bdiag}(\mathbf{f}_1, \ldots, \mathbf{f}_{N_{\mathrm{d}}})$, where $\mathbf{f}_j \in \mathbb{C}^{N_{\mathrm{e}}\times 1}$ is the weight vector belonging to the j-th TX DMA microstrip. The weights can be tuned by using the specific hardware employed at DMAs, such as varactor diodes [9]. For DMAs whose reconfigurable component is a varactor diode, the weights of the meta-elements must belong to the Lorentzian-constrained set

$$\Phi = \left\{\frac{\jmath + e^{\jmath\varphi}}{2}, \varphi \in [0, 2\pi]\right\}, \quad (5)$$

where φ is the tunable phase of the meta-elements. Moreover, the signal emitted from meta-elements experiences attenuation and a phase shift in the microstrip, similarly to propagation in waveguides. The diagonal elements of the attenuation matrix are given by

$$[\mathbf{P}_{\mathrm{TX}}]_{(j-1)N_{\mathrm{e}}+i,(j-1)N_{\mathrm{e}}+i} = e^{-\rho_{i,j}(\alpha_j + \jmath\beta_j)}, \quad (6)$$

where $\rho_{i,j}$ is the position of the i-th element in the j-th microstrip, α_j is the attenuation coefficient, and β_j is the wavenumber. With these definitions, the received signal obtained at the UE after applying the fully digital combiner $\mathbf{W}_{\mathrm{u}} \in \mathbb{C}^{N_{\mathrm{u}}\times N_{\mathrm{s}}}$, denoted by $\mathbf{y}_{\mathrm{u}} \in \mathbb{C}^{N_{\mathrm{s}}\times 1}$, is expressed as

$$\mathbf{y}_{\mathrm{u}} = \mathbf{W}_{\mathrm{u}}^{\mathrm{H}}\mathbf{H}_{\mathrm{u}}\mathbf{P}_{\mathrm{TX}}\mathbf{F}\mathbf{V}\mathbf{x} + \mathbf{W}_{\mathrm{u}}^{\mathrm{H}}\mathbf{n}_{\mathrm{u}}, \quad (7)$$

where $\mathbf{n}_{\mathrm{u}} \in \mathbb{C}^{N_{\mathrm{u}}\times 1}$ is the noise vector with entries that follow the complex Gaussian distribution with variance σ_{u}^2. Analogously, the weight matrix of the RX DMA is denoted by $\mathbf{W} \in \mathbb{C}^{N\times N_{\mathrm{d}}}$ which has a block-diagonal structure such that the blocks are the weight vectors of each misrostrip, i.e., $\mathbf{w}_j \in \mathbb{C}^{N_{\mathrm{e}}\times 1}$. The weights follow the Lorentzian constraint defined in (5). Additionally, the diagonal RX attenuation matrix $\mathbf{P}_{\mathrm{RX}} \in \mathbb{C}^{N\times N}$ is defined similar to (6). Hence, the received signal at the FD BS, $\mathbf{y}_{\mathrm{RX}} \in \mathbb{C}^{N_{\mathrm{d}}\times 1}$, is expressed as

$$\begin{aligned}\mathbf{y}_{\mathrm{RX}} &= \mathbf{W}^{\mathrm{H}}\mathbf{P}_{\mathrm{RX}}^{\mathrm{H}}\mathbf{H}_{\mathrm{R}}\mathbf{P}_{\mathrm{TX}}\mathbf{F}\mathbf{V}\mathbf{x} \\ &+ \mathbf{W}^{\mathrm{H}}\mathbf{P}_{\mathrm{RX}}^{\mathrm{H}}\mathbf{H}_{\mathrm{SI}}\mathbf{P}_{\mathrm{TX}}\mathbf{F}\mathbf{V}\mathbf{x} + \mathbf{W}^{\mathrm{H}}\mathbf{P}_{\mathrm{RX}}^{\mathrm{H}}\mathbf{n}_{\mathrm{RX}}, \quad (8)\end{aligned}$$

where $\mathbf{n}_{\mathrm{RX}} \in \mathbb{C}^{N\times 1}$ is the noise vector with entries that follow the complex Gaussian distribution with variance σ_{RX}^2. The received signal contains contributions from the target reflections and the SI. Since the SI channel is strong and the residual SI term could significantly degrade the target detection performance, precoders and combiners with SI mitigation capabilities should be designed. Note that the SI should be low at the output of the microstrips, before the LNAs and ADCs to prevent saturation and clipping.

III. PRECODER AND COMBINER DESIGN

We consider a tracking scenario such that the positions of the targets are estimated in a previous stage. This can be achieved by using a channel/parameter estimation algorithm (e.g., MUSIC) while using an SI-aware initial precoder and combiner [14]. With the estimated locations, the DL communication and target channels can be reconstructed. At this stage, the goal is to transmit DL data signals to the UE while simultaneously receiving the the reflections from the targets which are then used to re-estimate (i.e., track) the locations of the targets. Thus, the objective of the precoder and combiner design is to maximize the communication and sensing performance under residual SI, power and DMA weight constraints. This optimization problem can be expressed as

$$\begin{aligned} \underset{\mathbf{W}_{\mathrm{u}},\mathbf{W},\mathbf{F},\mathbf{V}}{\text{maximize}} \quad & R_{\mathrm{com}} + R_{\mathrm{s}} \\ \text{subject to} \quad & \left\| \left[\mathbf{W}^{\mathrm{H}}\mathbf{P}_{\mathrm{RX}}^{\mathrm{H}}\mathbf{H}_{\mathrm{SI}}\mathbf{P}_{\mathrm{TX}}\mathbf{F}\mathbf{V}\right]_{j,:} \right\|^2 \leq \gamma,\ \forall j, \\ & \|\mathbf{P}_{\mathrm{TX}}\mathbf{F}\mathbf{V}\|_{\mathrm{F}}^2 = P_{\mathrm{t}}, \\ & [\mathbf{w}_j]_i \in \Phi,\ \forall i,j, \quad [\mathbf{f}_j]_i \in \Phi,\ \forall i,j, \end{aligned} \tag{9}$$

where R_{com} and R_{s} are the communication and sensing metrics. For example, communication metric can be the rate and the sensing metric can be the radar signal-to-interference-plus-noise ratio (SINR). The residual SI threshold for each microstrip is denoted by γ, and the total transmit power is represented by P_{t}. The Lorentzian constraint on the DMA weights makes the problem non-convex, and the sensing metric and residual SI constraint create a coupling between the precoders and combiner at the FD BS.

A. Baseline Solution

We first describe the solution presented in [14], which utilizes two subproblems for the TX and RX DMA weights. Initially, the Lorentzian constraint and the attenuation inside microstrips are neglected, and the DMA weight vectors of each microstrip are selected from a DFT codebook. Then, the selected entries are projected onto the Lorentzian-constrained set. With these considerations, the first subproblem related to the TX DMA weights is expressed as

$$\underset{\tilde{\mathbf{F}}}{\text{maximize}} \quad \|\mathbf{H}_{\mathrm{R}}\tilde{\mathbf{F}}\|_{\mathrm{F}}^2, \qquad \text{subject to} \quad \tilde{\mathbf{f}}_j \in \mathcal{D},\ \forall j, \tag{10}$$

where $\mathcal{D}$ is the DFT codebook and the unit-modulus constrained TX weight matrix $\tilde{\mathbf{F}} \in \mathbb{C}^{N \times N_{\mathrm{d}}}$ is constructed as $\tilde{\mathbf{F}} = \mathrm{bdiag}(\tilde{\mathbf{f}}_1, \ldots, \tilde{\mathbf{f}}_{N_{\mathrm{d}}})$, where $\tilde{\mathbf{f}}_j \in \mathbb{C}^{N_{\mathrm{e}} \times 1}$ is selected from $\mathcal{D}$. The premise of this maximization problem is to optimize the weights for both communication and sensing performance since the UE is also a target. That is, the target channel $\mathbf{H}_{\mathrm{R}}$ contains the reflection from the UE. Given the TX weights, the optimization problem for the RX weight matrix $\tilde{\mathbf{W}} \in \mathbb{C}^{N \times N_{\mathrm{d}}}$ is formulated as

$$\underset{\tilde{\mathbf{W}}}{\text{maximize}} \quad \frac{\|\tilde{\mathbf{W}}^{\mathrm{H}}\mathbf{H}_{\mathrm{R}}\tilde{\mathbf{F}}\|_{\mathrm{F}}^2}{\|\tilde{\mathbf{W}}^{\mathrm{H}}\mathbf{H}_{\mathrm{SI}}\tilde{\mathbf{F}}\|_{\mathrm{F}}^2}, \qquad \text{subject to} \quad \tilde{\mathbf{w}}_j \in \mathcal{D},\ \forall j, \tag{11}$$

where the weights of each microstrip, $\tilde{\mathbf{w}}_j \in \mathbb{C}^{N_{\mathrm{e}} \times 1}$, is selected from $\mathcal{D}$. This optimization problem aims to find the weight vectors that have high correlation with the target channel while having low residual SI. Since the weight vectors are selected from a DFT codebook, which has limited codewords, the problems in (10) and (11) can be solved sequentially via a simple search. Since the entries do not satisfy the Lorentzian constraint, and the attenuation inside the microstrips is ignored, the authors project the unit-modulus weights to the set Φ by $[\mathbf{f}_j]_i = (\jmath + e^{\jmath \rho_{i,j}\beta_j}[\tilde{\mathbf{f}}_j]_i)/2$ and $[\mathbf{w}_j]_i = (\jmath + e^{\jmath \rho_{i,j}\beta_j}[\tilde{\mathbf{w}}_j]_i)/2$.

Note that this approach does not strongly enforce SI cancellation. To that end, the digital precoder can be divided into two parts as $\mathbf{V} = \mathbf{B}\mathbf{G}$, where $\mathbf{B} \in \mathbb{C}^{N_{\mathrm{d}} \times N_{\mathrm{n}}}$ is the null-space projection matrix and $\mathbf{G} \in \mathbb{C}^{N_{\mathrm{n}} \times N_{\mathrm{s}}}$ is the DL communication precoder. The null-space projection matrix is selected as $\mathbf{B} = [\mathbf{D}]_{:,N_{\mathrm{d}}-N_{\mathrm{n}}+1:N_{\mathrm{d}}}$, where $\mathbf{D}$ is the right singular vectors of the effective SI matrix $\mathbf{W}^{\mathrm{H}}\mathbf{P}_{\mathrm{RX}}^{\mathrm{H}}\mathbf{H}_{\mathrm{SI}}\mathbf{P}_{\mathrm{TX}}\mathbf{F}$. The number of columns selected for the null-space of the effective SI matrix should satisfy the constraint $N_{\mathrm{s}} \leq N_{\mathrm{n}} \leq N_{\mathrm{d}}$. Combiner and precoder for DL communication, i.e., $\mathbf{W}_{\mathrm{u}}$ and $\mathbf{G}$, can be designed as the N_{s} most dominant left and right singular vectors of the effective channel $\mathbf{H}_{\mathrm{u}}\mathbf{P}_{\mathrm{TX}}\mathbf{F}\mathbf{B}$, respectively. The number of null-space columns N_{n} should be selected as large as possible while keeping the residual SI observed at the output of each RX microstrip under γ.

The main drawbacks of this solution can be listed as follows: (i) the trade-off between the communication and sensing cannot be adjusted for the precoder design; (ii) the Lorentzian constraint is relaxed, and the codewords selected from a codebook with unit-modulus entries are projected onto the Lorentzian-constrained set; and (iii) the attenuation inside the microstrip is ignored. In the following, we overcome the mentioned shortcomings by proposing a strategy that optimizes the DMA weights under the Lorentzian constraint while considering the attenuation inside the microstrip.

B. Proposed Solution

We formulate the cost function for the optimization of the TX DMA weights as a weighted sum of the communication and sensing gains. Furthermore, we separately optimize the TX weights of each microstrip, which is equivalent to the original problem. Thus, the optimization problem for $\mathbf{f}_j$ is given as

$$\begin{aligned} \underset{\mathbf{f}_j}{\text{maximize}} \quad & w \left\|\bar{\mathbf{H}}_{\mathrm{u},j}\mathbf{P}_{\mathrm{TX},j}\mathbf{f}_j\right\|^2 + (1-w)\left\|\bar{\mathbf{H}}_{\mathrm{R},j}\mathbf{P}_{\mathrm{TX},j}\mathbf{f}_j\right\|^2 \\ \text{subject to} \quad & [\mathbf{f}_j]_i \in \Phi,\ \forall i, \end{aligned} \tag{12}$$

where $0 \leq w \leq 1$ is the convex weight that determines the communication and sensing trade-off. To define an equitable metric for sensing and communication we consider in (12) the normalized communication and target channels denoted by $\bar{\mathbf{H}}_{\mathrm{u}} \in \mathbb{C}^{N_{\mathrm{u}} \times N}$ and $\bar{\mathbf{H}}_{\mathrm{R}} \in \mathbb{C}^{N \times N}$, respectively. In (12), the

Algorithm 1 Conjugate gradient descent on manifold $\mathcal{U}$

```
Initialize: $\bar{\mathbf{f}}_j^{(0)}$, $\boldsymbol{\eta}^{(0)} = -\text{grad } f(\bar{\mathbf{f}}_j^{(0)})$, iteration $t = 0$
while not converged do
    $\bar{\mathbf{f}}_j^{(t+1)} = \bar{\mathbf{f}}_j^{(t)} + \xi^{(t)} \boldsymbol{\eta}^{(t)}$
    $\bar{\mathbf{f}}_j^{(t+1)} \leftarrow \bar{\mathbf{f}}_j^{(t+1)} \oslash \left|\bar{\mathbf{f}}_j^{(t+1)}\right|$
    $\boldsymbol{\eta}^{(t+1)} = -\text{grad } f(\bar{\mathbf{f}}_j^{(t+1)}) + \zeta^{(t)} \mathcal{T}_{\bar{\mathbf{f}}_j^{(t)} \to \bar{\mathbf{f}}_j^{(t+1)}}(\boldsymbol{\eta}^{(t)})$
    $t \leftarrow t + 1$
end while
Output: $\bar{\mathbf{f}}_j^{(t)}$
```

blocks that are in multiplicative form with $\mathbf{f}_j$ are obtained by $\bar{\mathbf{H}}_{\mathrm{u},j} = \left[\bar{\mathbf{H}}_{\mathrm{u}}\right]_{:,(j-1)N_{\mathrm{e}}+1:jN_{\mathrm{e}}}$, $\bar{\mathbf{H}}_{\mathrm{R},j} = \left[\bar{\mathbf{H}}_{\mathrm{R}}\right]_{:,(j-1)N_{\mathrm{e}}+1:jN_{\mathrm{e}}}$ and $\mathbf{P}_{\mathrm{TX},j} = \left[\mathbf{P}_{\mathrm{TX}}\right]_{(j-1)N_{\mathrm{e}}+1:jN_{\mathrm{e}},(j-1)N_{\mathrm{e}}+1:jN_{\mathrm{e}}}$. Although the cost function in (12) has a quadratic form, the Lorentzian constraint is non-convex. To circumvent this problem, we write the Lorentzian-constrained weights as [11]

$$\mathbf{f}_j = \frac{1}{2}\left(\boldsymbol{\jmath} + \bar{\mathbf{f}}_j\right), \tag{13}$$

where $\boldsymbol{\jmath} = [\jmath, \dots, \jmath]^{\mathrm{T}}$ and $[\bar{\mathbf{f}}_j]_i = e^{\jmath \varphi_{i,j}}$, $\forall i$. The part that needs to be optimized, i.e., $\bar{\mathbf{f}}_j \in \mathbb{C}^{N_{\mathrm{e}} \times 1}$ is separated in (13). Moreover, the entries of the optimization variable lie on the complex circle manifold $\mathcal{U}$ [17]. If we substitute the expression in (13) in (12), we obtain

$$\begin{aligned} \underset{[\bar{\mathbf{f}}_j]_i \in \mathcal{U},\, \forall i}{\text{maximize}} \quad f(\bar{\mathbf{f}}_j) = \frac{w}{4} \left\| \bar{\mathbf{H}}_{\mathrm{u},j} \mathbf{P}_{\mathrm{TX},j} \left(\boldsymbol{\jmath} + \bar{\mathbf{f}}_j\right) \right\|^2 \\ + \frac{1-w}{4} \left\| \bar{\mathbf{H}}_{\mathrm{R},j} \mathbf{P}_{\mathrm{TX},j} \left(\boldsymbol{\jmath} + \bar{\mathbf{f}}_j\right) \right\|^2. \end{aligned} \tag{14}$$

The cost function $f(\bar{\mathbf{f}}_j)$ still has a quadratic form, and (14) is an unconstrained optimization problem on the complex circle manifold. Therefore, this problem can be solved with manifold optimization algorithms such as conjugate gradient descent [10], [11], [17]. This is an iterative algorithm that can work on Riemannian manifolds. The steps of the algorithm are summarized in Algorithm 1. In this algorithm, the Riemannian gradient of the cost function is computed as grad $f(\bar{\mathbf{f}}_j) = \nabla_{\bar{\mathbf{f}}_j} f(\bar{\mathbf{f}}_j) - \mathrm{Re}\{\nabla_{\bar{\mathbf{f}}_j} f(\bar{\mathbf{f}}_j) \odot \bar{\mathbf{f}}_j^*\} \odot \bar{\mathbf{f}}_j$, where the Euclidean gradient of the cost function is expressed as

$$\begin{aligned} \nabla_{\bar{\mathbf{f}}_j} f(\bar{\mathbf{f}}_j) = \frac{w}{2} \left[\bar{\mathbf{H}}_{\mathrm{u},j} \mathbf{P}_{\mathrm{TX},j}\right]^{\mathrm{H}} \bar{\mathbf{H}}_{\mathrm{u},j} \mathbf{P}_{\mathrm{TX},j} \left(\boldsymbol{\jmath} + \bar{\mathbf{f}}_j\right) \\ \frac{1-w}{2} \left[\bar{\mathbf{H}}_{\mathrm{R},j} \mathbf{P}_{\mathrm{TX},j}\right]^{\mathrm{H}} \bar{\mathbf{H}}_{\mathrm{R},j} \mathbf{P}_{\mathrm{TX},j} \left(\boldsymbol{\jmath} + \bar{\mathbf{f}}_j\right). \end{aligned} \tag{15}$$

The iterative method starts with the update of the variable where the step size of the conjugate gradient method is denoted by $\xi^{(t)}$ for the t-th iteration. Next, the entries of the updated variable are normalized to keep them on the complex circle manifold. Finally, the conjugate search direction is updated with the Polak-Ribiere parameter $\zeta^{(t)}$, and the tangent transport operation defined as $\mathcal{T}_{\bar{\mathbf{f}}_j^{(t)} \to \bar{\mathbf{f}}_j^{(t+1)}}(\boldsymbol{\eta}^{(t)}) = \boldsymbol{\eta}^{(t)} - \mathrm{Re}\{\boldsymbol{\eta}^{(t)} \odot (\bar{\mathbf{f}}_j^{(t+1)})^*\} \odot \bar{\mathbf{f}}_j^{(t+1)}$ [17]. After solving the problem (14) with Algorithm 1, the DMA weights are recovered using (13).

We compute the digital precoder $\mathbf{V}$ by using the same approach followed in the previous subsection. That is, we separate it in two parts as $\mathbf{V} = \mathbf{BG}$, and use the N_{n} right singular vectors of $\mathbf{H}_{\mathrm{SI}} \mathbf{P}_{\mathrm{TX}} \mathbf{F}$. Then, the DL communication precoder and combiner can be computed by using the N_{s} singular vectors of $\mathbf{H}_{\mathrm{u}} \mathbf{P}_{\mathrm{TX}} \mathbf{FB}$. Note that we compute the digital precoder before computing the RX DMA weights, unlike [14], which removes the strong SI cancellation constraint on the RX DMA. For the design of the RX DMA combiner, we also separate the optimization of the weights of different microstrips. The main reason is that we are interested in the achieved gain and the residual SI observed at each microstrip. Similarly, we also separate the complex number and the unit-modulus parts of the RX DMA weight vectors as $\mathbf{w}_j = \frac{1}{2}(\boldsymbol{\jmath} + \bar{\mathbf{w}}_j)$. Then, we introduce the optimization problem on the complex circle manifold as

$$\underset{[\bar{\mathbf{w}}_j]_i \in \mathcal{U},\, \forall i}{\text{maximize}} \quad g(\bar{\mathbf{w}}_j) = \frac{\left\| (\boldsymbol{\jmath} + \bar{\mathbf{w}}_j)^{\mathrm{H}} \mathbf{A}_j \right\|^2}{\left\| (\boldsymbol{\jmath} + \bar{\mathbf{w}}_j)^{\mathrm{H}} \mathbf{B}_j \right\|^2}, \tag{16}$$

where $\mathbf{A}_j = \left[\mathbf{P}_{\mathrm{RX}}^{\mathrm{H}} \mathbf{H}_{\mathrm{R}} \mathbf{P}_{\mathrm{TX}} \mathbf{FV}\right]_{(j-1)N_{\mathrm{e}}+1:jN_{\mathrm{e}},:}$, and $\mathbf{B}_j = \left[\mathbf{P}_{\mathrm{RX}}^{\mathrm{H}} \mathbf{H}_{\mathrm{SI}} \mathbf{P}_{\mathrm{TX}} \mathbf{FV}\right]_{(j-1)N_{\mathrm{e}}+1:jN_{\mathrm{e}},:}$. Since this is an unconstrained manifold optimization problem, we use the conjugate gradient algorithm introduced in Algorithm 1. To that end, we compute the Euclidean gradient of the cost function $g(\bar{\mathbf{w}}_j)$ as

$$\begin{aligned} \nabla_{\bar{\mathbf{w}}_j} g(\bar{\mathbf{w}}_j) = & \frac{2\left\| (\boldsymbol{\jmath} + \bar{\mathbf{w}}_j)^{\mathrm{H}} \mathbf{B}_j \right\|^2 \mathbf{A}_j \mathbf{A}_j^{\mathrm{H}} (\boldsymbol{\jmath} + \bar{\mathbf{w}}_j)}{\left\| (\boldsymbol{\jmath} + \bar{\mathbf{w}}_j)^{\mathrm{H}} \mathbf{B}_j \right\|^4} \\ & - \frac{2\left\| (\boldsymbol{\jmath} + \bar{\mathbf{w}}_j)^{\mathrm{H}} \mathbf{A}_j \right\|^2 \mathbf{B}_j \mathbf{B}_j^{\mathrm{H}} (\boldsymbol{\jmath} + \bar{\mathbf{w}}_j)}{\left\| (\boldsymbol{\jmath} + \bar{\mathbf{w}}_j)^{\mathrm{H}} \mathbf{B}_j \right\|^4}. \end{aligned} \tag{17}$$

IV. NUMERICAL RESULTS

In this section, we evaluate the NF FD-ISAC performance of the proposed DMA weight optimization framework. We consider $K = 3$ NF targets, one of which is also a UE. The UE is equipped with a 2 antenna-ULA and a fully digital MIMO architecture. The bandwidth is set to 150 kHz to guarantee narrowband operation such that all DMA weights are attainable [9]. The TX and RX DMAs are placed on the xz-plane separated by 16λ. The microstrips on the TX and RX sides are placed with $\lambda/2$ spacing. We consider two different settings: (i) sub-THz operation with a carrier frequency $f_{\mathrm{c}} = 120$ GHz and 4 microstrips containing 512 meta-elements each with $\lambda/5$ spacing, and (ii) upper mid-band operation with a carrier frequency $f_{\mathrm{c}} = 13$ GHz and 32 microstrips containing 32 meta-elements each with $\lambda/2$ spacing. The attenuation parameters of the DMAs follow the design in [10]. The targets are deployed $5 - 25$ m away from the FD BS on the xy-plane. The errors in the initial position estimates follow a normal distribution with a variance of 1 m^2. The trade-off weight w in (14) is set to 0.5. We compare our results with the baseline method referred to as "Gavras2023" [14].

The DL spectral efficiency results at varying transmit power levels for the sub-THz setting are presented in Fig. 2. The proposed method provides significant performance gains compared to the benchmark. Additionally, we compare the proposed method with half-duplex communication only schemes with DMAs and regular arrays. The results reveal a performance loss in FD-ISAC designs, primarily due to the limited number of microstrips (i.e., RF chains) in this setting. Next, we examine

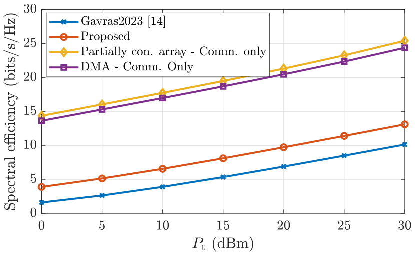

Fig. 2. Spectral efficiency vs transmit power for the sub-THz setting.

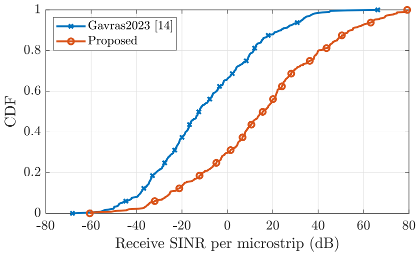

Fig. 3. CDF of the receive radar SINR achieved at the output of DMA microstrips at $P_\mathrm{t} = 20$ dBm for the sub-THz setting.

the received radar SINR per microstrip, as shown in Fig. 3. The proposed method achieves substantial improvements over the benchmark, thanks to the optimization on the Lorentzian-constrained set, which enhances SI suppression and gain. The spectral efficiency and radar SINR results for the upper mid-band setting are illustrated in Fig. 4 and Fig. 5, respectively. The proposed method outperforms the benchmark in both metrics. Note that the performance gap with communication-only schemes is reduced in this setting, owing to the larger number of available microstrips. The radar SINR gap between the proposed method and the benchmark is reduced since the availability of more RF chains enables effective SI suppression through digital precoding. Finally, it is worth noting that the proposed method offers flexibility in adjusting the communication and sensing trade-off via weighted precoder optimization.

V. CONCLUSION

In this paper, we proposed a DMA weight optimization method for NF FD-ISAC systems. We exploited a Riemannian manifold optimization framework to optimize the DMA weights under Lorentzian constraint while maximizing communication and sensing gains and mitigating SI. Simulation results showed significant improvements in ISAC performance and SI suppression compared to the benchmark, both for sub-THz and upper mid-band scenarios.

REFERENCES

[1] N. González-Prelcic, M. F. Keskin, O. Kaltiokallio, M. Valkama, D. Dardari, X. Shen, Y. Shen, M. Bayraktar, and H. Wymeersch, "The integrated sensing and communication revolution for 6G: Vision, techniques, and applications," *Proc. IEEE*, 2024.

[2] C. B. Barneto, S. D. Liyanaarachchi, M. Heino, T. Riihonen, and M. Valkama, "Full duplex radio/radar technology: The enabler for advanced joint communication and sensing," *IEEE Wireless Commun.*, vol. 28, no. 1, pp. 82–88, 2021.

[3] C. B. Barneto, T. Riihonen, S. D. Liyanaarachchi, M. Heino, N. González-Prelcic, and M. Valkama, "Beamformer design and optimization for joint communication and full-duplex sensing at mm-Waves," *IEEE Trans. Commun.*, vol. 70, no. 12, pp. 8298–8312, 2022.

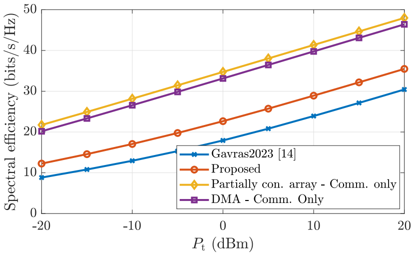

Fig. 4. Spectral efficiency vs transmit power for the upper midband setting.

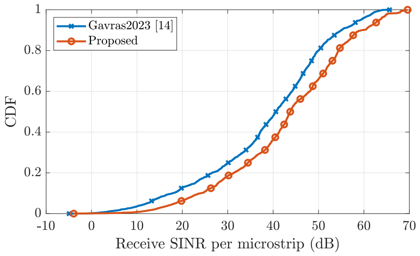

Fig. 5. CDF of the receive radar SINR achieved at the output of DMA microstrips at $P_\mathrm{t} = 0$ dBm for the upper midband setting.

[4] M. Bayraktar, N. González-Prelcic, and H. Chen, "Hybrid precoding and combining for mmWave full-duplex joint radar and communication systems under self-interference," in *Proc. IEEE Int. Conf. Commun. (ICC)*, 2024, pp. 1–6.

[5] M. Bayraktar, N. González-Prelcic, H. Chen, and C. J. Zhang, "Truly full-duplex integrated sensing and single-user communication at mmWave," in *Proc. IEEE 25th Int. Workshop Signal Process. Advances Wireless Commun. (SPAWC)*, 2024, pp. 116–120.

[6] B. Zhao, C. Ouyang, Y. Liu, X. Zhang, and H. V. Poor, "Modeling and analysis of near-field ISAC," *IEEE J. Sel. Topics Signal Process.*, vol. 18, no. 4, pp. 678–693, 2024.

[7] H. Li, Z. Wang, X. Mu, P. Zhiwen, and Y. Liu, "Near-field integrated sensing, positioning, and communication: A downlink and uplink framework," *IEEE J. Sel. Areas Commun.*, vol. 42, no. 9, pp. 2196–2212, 2024.

[8] D. Galappaththige, S. Zargari, C. Tellambura, and G. Y. Li, "Near-field ISAC: Beamforming for multi-target detection," *IEEE Wireless Commun. Lett.*, vol. 13, no. 7, pp. 1938–1942, 2024.

[9] N. Shlezinger, G. C. Alexandropoulos, M. F. Imani, Y. C. Eldar, and D. R. Smith, "Dynamic metasurface antennas for 6G extreme massive MIMO communications," *IEEE Wireless Commun.*, vol. 28, no. 2, pp. 106–113, 2021.

[10] H. Zhang, N. Shlezinger, F. Guidi, D. Dardari, M. F. Imani, and Y. C. Eldar, "Beam focusing for near-field multiuser MIMO communications," *IEEE Trans. Wireless Commun.*, vol. 21, no. 9, pp. 7476–7490, 2022.

[11] S. F. Kimaryo and K. Lee, "Downlink beamforming for dynamic metasurface antennas," *IEEE Trans. Wireless Commun.*, vol. 22, no. 7, pp. 4745–4755, 2022.

[12] G. Lan, M. F. Imani, P. d. Hougne, W. Hu, D. R. Smith, and M. Gorlatova, "Wireless sensing using dynamic metasurface antennas: Challenges and opportunities," *IEEE Commun. Mag.*, vol. 58, no. 6, pp. 66–71, 2020.

[13] Q. Yang, A. Guerra, F. Guidi, N. Shlezinger, H. Zhang, D. Dardari, B. Wang, and Y. C. Eldar, "Near-field localization with dynamic metasurface antennas," in *Proc. IEEE Int. Conf. Acoust., Speech, Signal Process. (ICASSP)*, 2023, pp. 1–5.

[14] I. Gavras, M. A. Islam, B. Smida, and G. C. Alexandropoulos, "Full duplex holographic MIMO for near-field integrated sensing and communications," in *Proc. 31st Eur. Signal Process. Conf. (EUSIPCO)*, 2023, pp. 700–704.

[15] I. Gavras and G. C. Alexandropoulos, "Simultaneous near-field THz communications and sensing with full duplex metasurface transceivers," in *Proc. IEEE 25th Int. Workshop Signal Process. Advances Wireless Commun. (SPAWC)*, 2024, pp. 126–130.

[16] S. W. Ellingson, "Path loss in reconfigurable intelligent surface-enabled channels," in *Proc. IEEE 32nd Annu. Int. Symp. Pers., Indoor, Mobile Radio Commun. (PIMRC)*, 2021, pp. 829–835.

[17] P.-A. Absil, R. Mahony, and R. Sepulchre, *Optimization algorithms on matrix manifolds*. Princeton University Press, 2008.